Title

High-brightness beam tests of the very high frequency gun at the Advanced Photo-injector EXperiment test facility at the Lawrence Berkeley National Laboratory

Journal

Review of Scientific Instruments, 90(3)

ISSN

0034-6748

Authors

Sannibale, F

Filippetto, D

Qian, H

et al.

Publication Date

2019-03-01

DOI

10.1063/1.5088521

Peer reviewed

High-brightness beam tests of the Very High Frequency Gun at the Advanced Photo-injector Experiment test facility at the Lawrence Berkeley National Laboratory

F. Sannibale,[1,*] D. Filippetto,[1] H. Qian,[1,†] C. Mitchell,[1] F. Zhou,[2] T. Vecchione,[2] R. K. Li,[2] S. Gierman,[2] and J. Schmerge[2]

[1] *Lawrence Berkeley National Laboratory, 1 Cyclotron Road, Berkeley, CA 94720, USA*
[2] *SLAC, Menlo Park, CA 94025, USA*

(Dated: March 27, 2019)

The very-high-frequency gun (VHF-Gun) is a new concept photo-injector developed and built at the Lawrence Berkeley National Laboratory (LBNL) for generating high-brightness electron beams capable of driving X-ray FELs at MHz-class repetition rates. The gun that purposely uses established and mature radiofrequency and mechanical technologies, has demonstrated over the last many years the capability of reliably operating in continuous wave mode at the design accelerating fields and required vacuum and mechanical performance. The results of VHF-Gun technology demonstration were reported elsewhere [F. Sannibale, *et al.*, Phys. Rev. ST - Accel. and Beams 15, 103501 (2012)], here in this paper we provide and analyze examples of the experimental results of the first high-brightness beam tests performed at the Advanced Photo-injector EXperiment (APEX) test facility at LBNL that demonstrated the gun capability of delivering the beam quality required for driving high repetition rate X-ray FELs.

PACS numbers: 29.25.Bx, 29.27.Bd, 29.27.Eg, 41.60.Cr

I. INTRODUCTION

Since their invention in 1971 [1], free electron lasers (FELs) underwent through a tremendous development and are considered among the most successful accelerator-based applications of our time. In particular, in the last couple of decades, FELs based on linear accelerators demonstrated the revolutionary capability of delivering femtosecond X-ray pulses with many orders of magnitude higher intensity and peak brightness than any other existing source [2–8]. The availability of such photon facilities opened the way to new classes of experiments probing nature with unprecedented spatial and temporal resolution. This successful story was made possible by the challenging development of high-brightness electron guns capable of generating electron beams with sub-micron normalized emittances and tens to hundreds of pC charges per bunch [9]

One common characteristic of all presently operating X-ray FELs is that they are based on electron accelerators operating at a relatively low duty-cycle with pulses or train of pulses generated at repetition rates limited to a few hundred Hz. Such a mode of operation dramatically limits the goals of a strong and steadily growing scientific community asking for the extension of the formidable X-ray FEL performance to MHz-class repetition rates with photon pulses equally spaced in time [10]. The accelerator community responded to this call by proposing higher duty cycle upgrades for existing facilities [11], and several new high duty-cycle FEL schemes [12–15]. Two in this last category, LCLS-II in US and SHINE in China, have been approved and are presently under construction [16, 17].

The high repetition rate requirement has a profound impact on the technology choice for most of the FEL accelerator systems, and in particular for the electron gun. While at the time of the first proposals, the superconducting linac technology was essentially ready for the high duty-cycle operation, the same could not be said for the electron source. In fact, the successful room-temperature GHz radiofrequency (RF) electron gun technology used in the existing low duty-cycle FELs [9], could not be scaled up to the required high rates because of the excessive heat load that those regimes would impose on the gun cavity walls [18]. In the attempt of solving that problem, a number of groups around the world started to develop new gun schemes based on technologies, such as direct current (DC) and super-conducting RF, potentially capable of high duty cycle operation. A review and description of these different schemes can be found elsewhere [19]. Our group at the Lawrence Berkeley National Laboratory (LBNL) took a different route developing the very-high-frequency gun (VHF-Gun), a novel-scheme lower-frequency room-temperature RF photo-gun [20–24] capable of continuous wave (CW) operation and optimized for the performance required by MHz-class X-ray FELs [25, 26]. The Advanced Photo-injector EXperiment (APEX), an injector test facility, was built at LBNL for demonstrating the VHF-Gun performance. In particular, a two-months beam test campaign in 2016 was dedicated to the verification of the VHF-Gun capability of delivering beams with the characteristics required by X-ray FELs.

In this paper, examples of the high-brightness FEL-quality results successfully demonstrated during such a campaign are presented and discussed.

Based on this positive results, several high repetition

* email address: FSannibale@LBL.gov
† Now at DESY, 15738 Zeuthen, Germany

TABLE I. APEX Phase-II Main Parameters

Parameter	Demonstrated Value
Gun frequency	185.714 MHz
Gun operation mode	CW
Max beam energy at gun exit	$\sim$ 0.8 MeV
Nominal operational energy	0.75 MeV
Field at the cathode @ 0.75 MeV	$\sim$ 20 MV/m
Buncher frequency	1.3 GHz
Buncher cells	2
Buncher operation mode	CW
Max buncher voltage	240 kV
Linac section frequency	1.3 GHz
Linac operation mode	pulsed
Linac max repetition rate	10 Hz
Max linac section voltage	$\sim$ 8 MV
Number of linac sections	2
Max beam energy at linac exit	$\sim$ 17 MeV
Transverse deflecting cavity frequency	1.3 GHz
Transverse deflecting cavity cells	1
Transverse focusing	solenoids & quadrupoles
Beam diagnostics suite characterization capability	6D phase space

rate FEL proposals are now planning to use a VHF-Gun-like electron source in their schemes, including LCLS-II and SHINE, the two facilities presently under construction. For the LCLS-II case in particular, a second VHF-Gun (a close version of the original one) was built by LBNL and delivered to SLAC.

It is worth remarking that an electron source with the VHF-gun characteristics can be readily used in other high-repetition rate, high-brightness applications such as, for example, electron cooling schemes; infrared to extreme ultra-violet FELs; inverse Compton scattering X-ray or gamma sources; and ultrafast electron diffraction (UED) and microscopy (UEM). As a matter of fact, the original VHF-Gun, after the FEL tests described in this paper was fully dedicated to the operation of HiRES [27], the LBNL MHz-class UED facility.

Several options to further improve the brightness performance of the VHF-Gun technology have been recently proposed [28], and an explorative study to evaluate the feasibility of such proposals is underway.

II. THE VHF-GUN AND APEX, THE ADVANCED PHOTO-INJECTOR EXPERIMENT

A detailed description of the VHF-Gun and of its characteristics can be found elsewhere [21, 22], here, for the reader convenience, only the main relevant features of the gun are summarized. In the VHF-Gun scheme, the electron bunches are generated by laser-induced photoemission on high quantum efficiency (QE) semiconductor cathodes [24, 29]. The particles are then accelerated over a 4 cm gap up to the nominal operational energy of 750 keV by the 20 MV/m electric field excited in a room-temperature copper RF cavity operating in CW mode and resonating at 185.714 MHz (the 7-th sub-harmonic of 1.3 GHz and close to the 8-th of 1.5 GHz, the dominant superconducting linac technologies). The beam repetition rate of the VHF-Gun is 1 MHz as typically required by the proposed and in-construction high duty cycle x-ray FELs, but with the proper cathode driving laser, it could be in principle as high as the gun RF frequency. The relatively low RF frequency choice allowed addressing the two most challenging requirements imposed by the high-repetition rate: the capability of the gun of running in CW mode; and the achievement of the extremely low vacuum pressures necessary to operate reactive and delicate semiconductor photocathodes with acceptable lifetimes (the high QE offered by these materials is necessary to generate the high average current required by high-duty cycle FEL applications). At the VHF frequencies (30 to 300 MHz), the resonant cavity is large enough to lower the power density on the cavity walls to a level where conventional cooling techniques can be used to run in CW mode, while maintaining the high accelerating fields required for the high brightness performance [30, 31]. Also, the long wavelength allows for large apertures on the cavity walls with negligible field distortion. Such apertures provide the vacuum conductance necessary to achieve the desired low pressures. In designing the VHF-Gun, a particular attention was placed on using mature and established RF and mechanical technologies to generate a reliable device capable of providing the continuity of operation required by a user facility.

APEX, the Advanced Photo-injector EXperiment at the LBNL is an electron injector test facility that was built for characterizing the VHF-Gun performance. The APEX project was organized in 3 stages (Phase 0, I and II), with the first two dedicated to the characterization and testing of the VHF-Gun technology, cathode testing and electron beam characterization at the gun energy [21, 23, 24]. In Phase II, a buncher and a linac were added to the VHF-Gun to compress and accelerate the beam to more relativistic energies, reducing space charge forces and allowing to characterize the gun/injector beam brightness and bunch length compression performance.

Figure 1 shows a CAD layout and Figure 2 a panoramic photo of the APEX Phase-II beamline installed at LBNL. The beamline main parameters are summarized in Table I. The vacuum loadlock that allows replacing cathodes without breaking vacuum (based on the INFN-LASA design [32]), and the VHF-Gun are visible in the left part of Fig. 1. Following the direction of the beam exiting the gun, a first focusing solenoid is encountered

TABLE II. Beam parameter goals and achieved values

Parameter	Goal	Measured
Beam energy at APEX exit (MeV)	≥ 10	15-16.5
Charge per bunch (pC)	≥ 20	20-25
Normalized hor. and vert. projected emittance (95% of the beam) (μm)	≤ 0.25	$\lesssim 0.25$
Bunch peak current (A)	≥ 5	5-9
High-order r.m.s. energy spread (keV)	$\lesssim 5$	~ 5*

*Estimated (See Section IV A).

followed by the 1.3 GHz CW buncher (an LBNL-designed room-temperature 2-cell cavity [33]), and by a second focusing solenoid. This set of components is then followed by a pulsed linac composed by two 1 m long 1.3 GHz 7-cell normal-conducting accelerating sections, (a modified version of the Argonne AWA standing-wave structures [34]). The central cell where the RF power is fed into these accelerating sections, was modified with respect to the original design by adding a second symmetrical coupler and two dummy ports to eliminate dipole and quadrupolar RF field components that could harm the beam quality [35]. Originally, the layout included a third accelerating section but due to a delayed delivery by the manufacturer and to schedule constraints, this section was not installed. As it will discussed later in Section IV A, this was not a painless decision because the consequent reduction of the maximum energy available at the APEX exit significantly increased the importance of space charge effects on the beam test results. Downstream of the linac, a beam diagnostics suite is located [36] with 6-D beam phase-space characterization capability. The set of systems includes emittance monitors, a spectrometer, and a 1.3 GHz transverse deflecting cavity (TCav) based on a Cornell design [37]. Beam position monitors, steering coils, fluorescent screens, and charge monitors properly distributed along the beamline complete the diagnostic system.

As shown in Table I, the VHF-Gun and the buncher run in CW mode, while the linac operates in pulsed mode with 10 Hz repetition rate. The rationale behind this configuration choice is that the electron beam 6-D brightness (the main quantity to be demonstrated at APEX) is a single bunch beam property that can be measured at any repetition rate. The use of a pulsed room temperature copper linac allowed for a strong cost reduction and simplification of the system.

III. HIGH BRIGHTNESS BEAM TESTS RESULTS

This section is devoted to the description of some of the results of the APEX two-month beam measurement campaign dedicated to the demonstration of the VHF-Gun capability of delivering the high-brightness beams required by an X-ray FEL.

The requirements for one of the possible modes of operation of the LCLS-II were selected as target for these tests in the framework of a collaboration with that project. LCLS-II will operate in several modes with charges per bunch ranging from a few tens to a few hundreds of pC. The VHF-Gun had already demonstrated steady production of bunches with hundreds of pC at MHz repetition rate [24], but for these tests, the 20 pC charge per bunch was chosen. At this relatively low charge, the effects of magnetic and RF field aberrations on the final beam quality are less masked by dominant space charge forces, making the optimization process particularly challenging. The goal values for the main beam parameters were defined by start-to-end simulations using the LCLS-II FEL layout [38]. Table II shows the resulting parameter goals and the values demonstrated during these beam tests.

The measurement examples reported and discussed in the following sections were performed with the gun operating at an energy of 630 keV, instead of the nominal 750 keV, due to a temporary (subsequently resolved) limitation in the RF distribution system. It is worth remarking that the lower gun energy, and consequently the lower field at the cathode (16.8 MV/m instead of 20), made the demonstration of the goal values more challenging.

A. Cathode and laser pulse measurements

Multi-alkali antimonide CsK_2Sb cathodes produced at LBNL were used for the tests [39]. Low charge emittance measurements at APEX of several such cathodes revealed thermal emittances at 515 nm ranging between 0.5 and 0.6 μm/mm r.m.s. (where r.m.s. stays for root mean square). The initial QEs, measured at the same wavelength, ranged between 2% to 5% with a typical 1/e QE lifetime of $\sim$ 3 days [29].

The laser pulse, driving the photo-emission from the cathode, was shaped in the transverse plane by cutting the quasi-Gaussian transverse distribution at $\sim$ 1 sigma by a circular aperture located at an image plane along the laser beamline. The final part of such beamline included a 'virtual cathode' branchline where an image of the laser reproducing the one on the actual cathode was created for diagnostics and optimization use. Figure 3 shows a virtual cathode image showing the laser pulse transverse profile used during the measurements described in this section. The image shows a nearly tophat distribution with $\sim$ 170 μm r.m.s. size in both horizontal and vertical planes. The figure also shows the presence of some intensity modulation on the flattop, and a low intensity halo surrounding the core of the distribution, indication of a profile not completely optimized.

The laser pulse was also shaped longitudinally by using a stack of 5 BBO (barium borate) birefringent crystals with different thickness to subsequently split, delay and overlap 32 smaller copies of the original quasi-Gaussian laser pulse with $\sim$ 800 fs FWHM length. In this way a quasi trapezoidal distribution with ps rise and

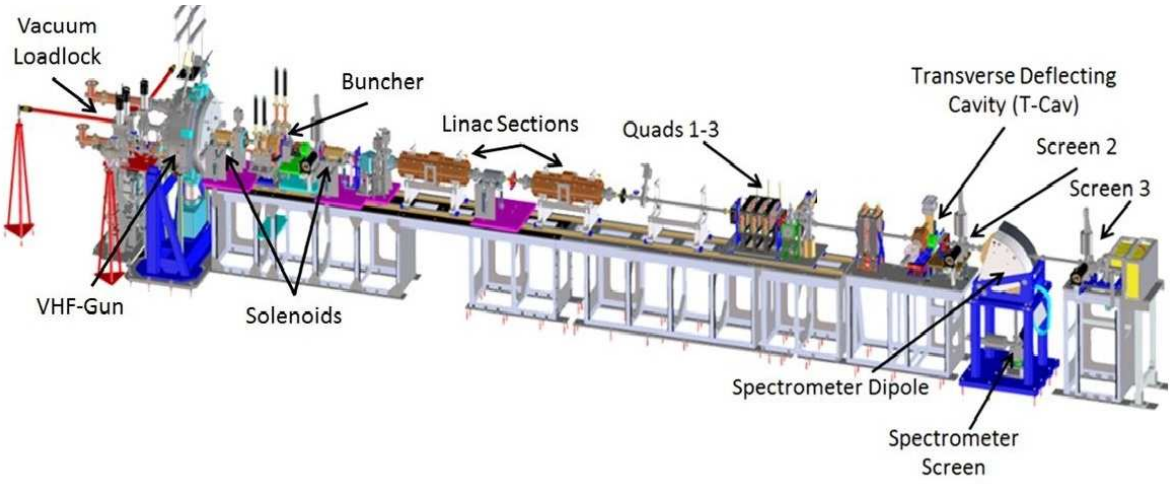

FIG. 1. APEX Phase II layout with main components in evidence.

FIG. 2. Panoramic photo of APEX Phase-II as installed in early 2016 in the Beam Test Facility at the Lawrence Berkeley National Laboratory.

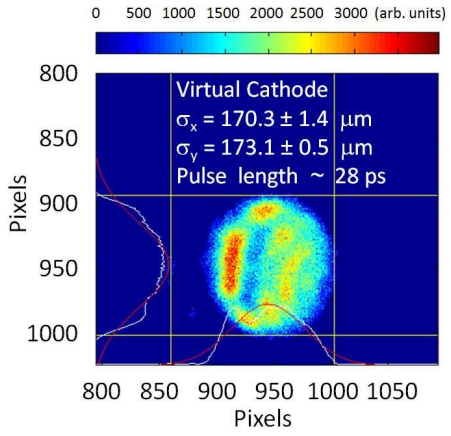

FIG. 3. 'Virtual cathode' image of the typical laser beam transverse profile used during the measurements described in the paper.

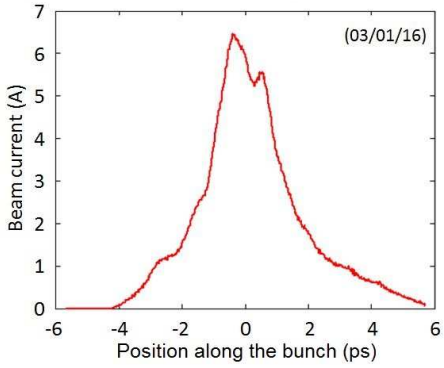

FIG. 4. The longitudinal beam profile of the 20 pC beam during the tests described in Section III as measured using the transverse deflecting cavity in combination with Screen 3 (see Fig. 1 for component positions).

fall times and $\sim$ 28 ps flattop was obtained. No diagnostics was available to directly measure the longitudinal distribution of the laser, so each crystal angle was individually adjusted to split the pulse into two equally intense pulses. A final optimization of the shape was subsequently attempted by tuning the crystal angles looking at the longitudinal profile of the electron beam at the end of the APEX beamline (by using the transverse deflecting cavity in combination with one of the fluorescent screens). The electron beam distribution measured during the 20 pC/bunch beam tests described in this section is visible in Fig. 4. The modulation visible on the beam profile clearly indicates that the laser pulse shape at the cathode was also not completely optimized. The figure also shows the effect of bunch compression and acceleration along the buncher and linac that, in combination with space charge forces, transformed the quasi-

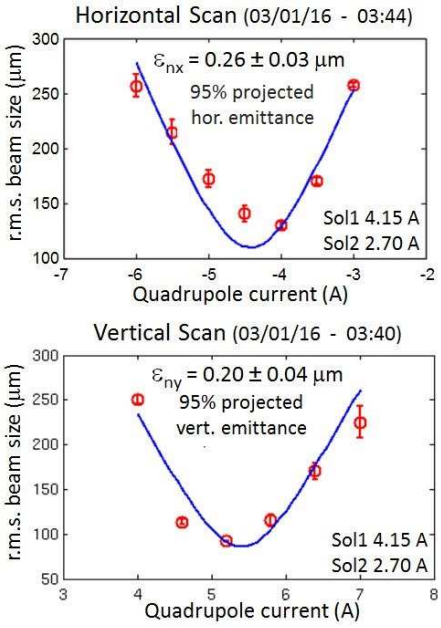

FIG. 5. Example of horizontal and vertical projected emittance measurement of a 20 pC, 15.7 MeV beam performed by scanning Quad 3 current and measuring beam sizes on Screen 3 (see Fig. 1 for component positions).

trapezoidal distribution at the cathode into a shorter distribution with elongated edges.

B. Transverse plane measurements

Figure 5 shows a measurement of the projected transverse emittance of the 20 pC beam with the longitudinal profile showed in Fig. 4. The well-known 'quad-scan technique' [40] was used for the measurement. The field in Quad 3 was varied by changing in steps the current in the quadrupole coils while collecting for each of such steps the projected transverse beam profiles on Screen 3 (see Fig.1 for the position of such components). The r.m.s. beam sizes for each of the transverse planes were then calculated directly from the measured distributions and the values of the projected normalized emittances for both the horizontal and vertical planes was then extracted by properly fitting and analyzing the data. From the figure it can be seen that the measured value compares well with the target value of 0.25 μm indicated in Table II. The figure also shows that the fit in both planes does not perfectly represent all the measured data points. This last point will be now further discussed.

Figure 6, which shows the details of the vertical measurement in Fig. 5, is divided in six parts each containing the beam image at the screen for the different settings of the quadrupole current. Every of such parts contains in the left the raw beam image as seen at the screen, and in the right a magnification of the area occupied by the beam where it is possible to observe the details of the electron distribution. This last part also includes the projections of the beam distributions in the horizontal and vertical planes (white lines) and their respective Gaussian fits (red lines). It can be seen that in general, the Gaussian fit well represents the actual beam distribution, but also, after a more accurate observation, that it fails to follow the tails of the distribution. This is clearly visible in the inset of Fig. 6 where a further magnification of the tail of one of the images shows how the red and white lines poorly overlap. This behaviour of the fit is a direct consequence of the presence of the beam halo clearly visible around the beam core in all the magnified beam images. To evaluate the effect of the halo on the measurement results, an alternate approach for the data analysis was used. In Fig. 7 the vertical measurement already shown in Fig. 5 is now analyzed using two different methods. On the top part of the figure, the beam sizes for each of the quadrupole settings are derived by fitting the vertical projection of the beam distribution with a Gaussian function and taking the standard deviation of the fit as the vertical r.m.s. size of the beam. The bottom part of the figure contains the same plot already showed in Fig. 5, where the the r.m.s. values of the vertical projections were calculated directly from the raw data. The exact same analysis algorithm was then used in both cases to extract the emittance values. When comparing the results between these two approaches, two clear differences are evident: in the Gaussian fit case, the fitting function used in the algorithm represents the data much more accurately, and the measured emittance value obtained by this method is $\sim 35\%$ smaller with respect to the other case. These differences are largely due to the presence of the beam halo visible in the images of Fig. 6. As noted earlier, the Gaussian function fails to fit the beam tails or, in other words, in the Gaussian fit case, the emittance of the beam is measured with the contribution from the particles in the halo mostly ignored. This result indicates that if the beam halo is reduced (for example by reducing/removing the halo in the laser pulse at the cathode) the overall emittance of the beam can significantly decrease.

Similarly to the vertical scan case described above, Figure 8 shows the details of the emittance measurement this time for the horizontal plane. The analysis of this case reveals an interesting feature that will be now discussed. The top part of Fig. 5 shows that during the measurement, the smallest horizontal beam sizes were obtained when the quadrupole current was set to -4 and -4.5 A. At these current values, the magnified image of the beam in Fig. 8 shows a projected horizontal distribution with an irregular elongated region in the center. This shape is consistent with the existence of a longitudinal to transverse position correlation that is visible only when the horizontal beam size becomes small enough to not mask the horizontal displacement existing between the head and the tail of the beam. Such a correlation, which can be generated for example by a misaligned beam inside the linac sections, leads to an overestimate of the measured

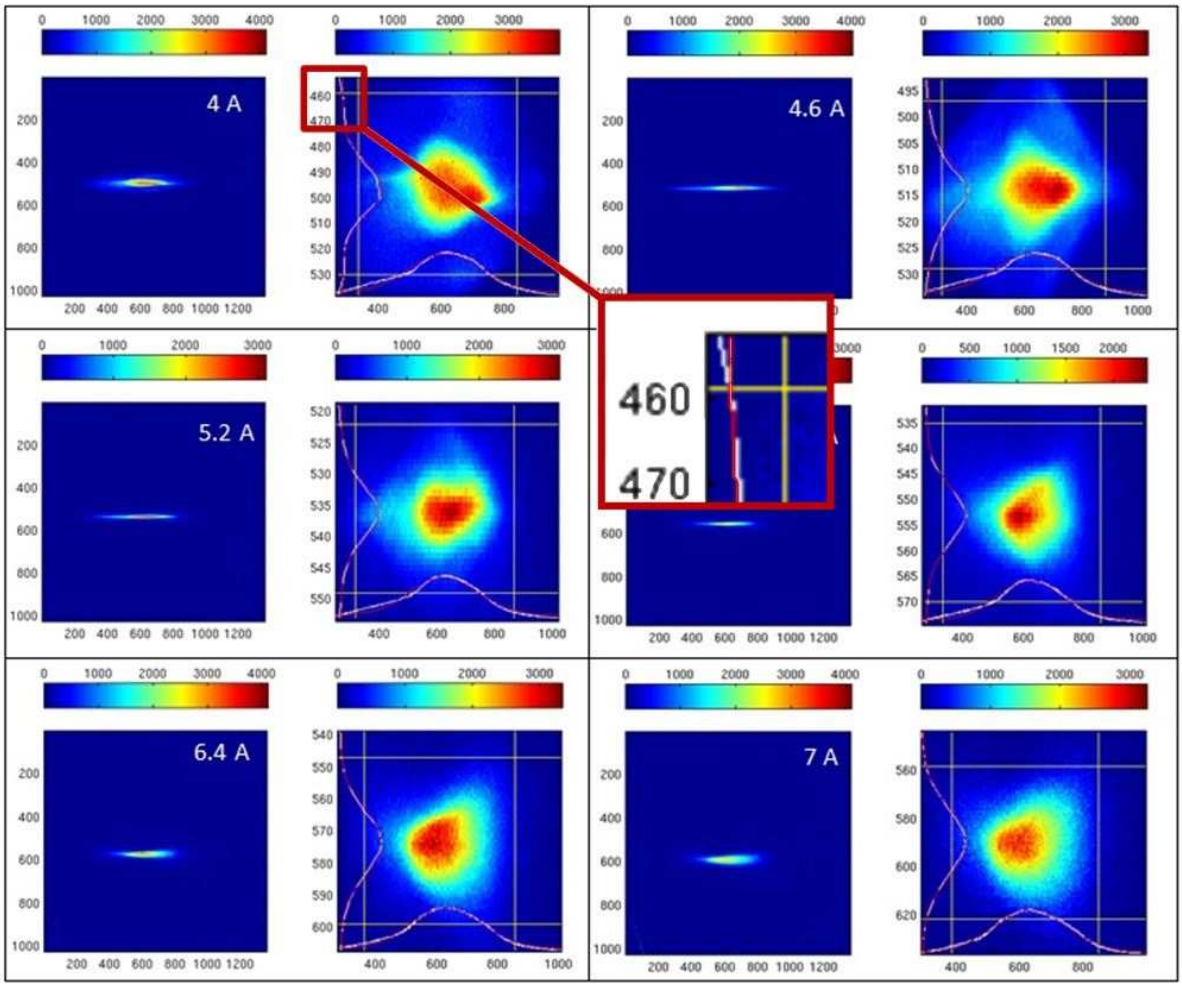

FIG. 6. Details of the vertical quadrupole scan measurement shown in Fig. 5. The Figure is divided in six parts, one for each of the settings of the quadrupole current. The single part contains the raw image of the beam at Screen 3 on the left, and a magnified version of it on the right. In the latter, white lines shows the projection profiles for each of the plains, and red lines the Gaussian fit of such profiles. The inset shows a magnified view of the tail of one of the projections in the vertical plane. The units for the image axes are pixels (pixel size 16.19 μm), while the intensity values associated with colour scale are in arbitrary units.

emittance and contributes the non-perfect fit of the data visible in top part of Fig. 5. Once more and similarly to the vertical case, these results indicate that although the present results already satisfy the goals, a further injector optimization can potentially lead to smaller emittance values.

C. Longitudinal plane measurements

Figure 9 shows an example of a typical longitudinal phase space measurement performed during the campaign described in this paper. The image was obtained by using the well-known technique [41] where the Transverse Deflecting Cavity imprints a linear horizontal-momentum to longitudinal-position correlation along the beam, while the Spectrometer Dipole downstream of the cavity creates energy dispersion in the vertical plane (see Fig. 1 for component positions). In this way, after propagation, the beam forms an image on the Spectrometer Screen of its longitudinal phase space. The top part of Fig. 9 shows the raw image of the beam at the screen and the orientation of the energy and time (longitudinal position) axes. Also visible are the profiles showing the respective projections of the beam distribution on such axes. The bottom part of the figure shows the phase-space distribution that is obtained from the same beam when the linear and quadratic correlations between the temporal and energy planes are analytically removed. The r.m.s value of the projection of this last distribution on the energy axis is what is referred in Table II as the *high − order r.m.s. energy spread*. In the typical FEL application, the high-order r.m.s. energy spread is a convenient figure of merit to use for characterizing the quality of the energy part of the longitudinal phase space. This is justified by the fact that in such facilities, both

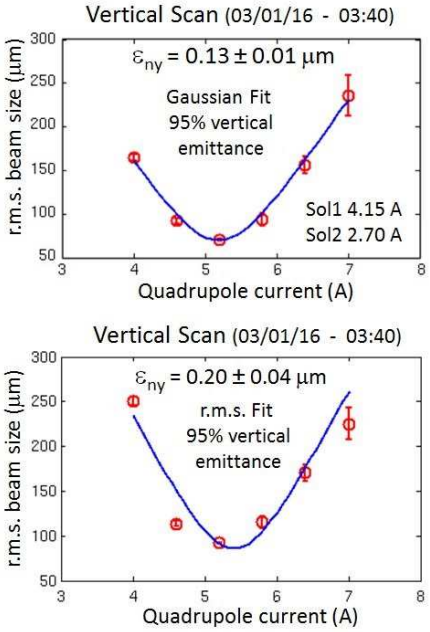

FIG. 7. In this figure the vertical scan of the measurement shown in Fig. 5 is analyzed by using two different methods. In the top part of the figure the projections of the beam distribution on the screen are fitted by a Gaussian function and the standard deviation of the Gaussian fit is taken as the vertical beam size. In the bottom part, the beam size is represented by the r.m.s value calculated directly from the measured vertical distribution. The two-cases comparison is discussed in the text.

linear and quadratic correlation terms can be compensated, the first for example, by dephasing part of the linac sections, and the second by the harmonic cavity linearizers [42] that are typically present along the linac. Once these two terms are corrected, the remaining higher order correlations are the ones that will ultimately limit the capability of compressing the bunch in the downstream linac magnetic compressors and need to be minimized.

The measurement shown in Fig. 9 was performed on a 20 pC beam with 16.2 MeV energy and a peak current of $\sim$ 5.2 A. The high-order r.m.s energy spread value calculated from the distribution in the bottom part of the figure is 14.3 $\pm$ 0.3 keV. This figure overestimates the actual value because it includes the contributions due to the spectrometer resolution, the energy spread induced by the transverse deflecting cavity, and the energy spread increase due to residual space charge forces associated to the relatively low energy of the beam at APEX. The deflecting cavity contribution scales linearly with the r.m.s. beam size at the cavity position with a scaling factor that depends on the amplitude of the RF field in the cavity. For the specific case of the measurement in Fig. 9, σ_x, the horizontal r.m.s. beam size at the deflecting cavity position, was 345 μm with a scaling factor of 2.2 keV per each 100 μm of σ_x generating a contribution to the energy spread of 7.6 keV. Simulations (details in Section IV A) estimated that the effect of the residual space charge forces was to increase the measured value of the high-order r.m.s. energy spread by almost 60%. The contribution of the spectrometer resolution could not be evaluated because it depends on the vertical r.m.s. beam size at the Spectrometer Screen position and that quantity not was not measured during this specific measurement.

An upper limit for the value of the high-order r.m.s. energy spread can be extracted from a total energy spread measurements at the APEX spectrometer. Figure 10 shows one of these measurements for a 20 pC beam compressed to a peak current of $\sim$ 6 A and accelerated at an energy of 15.7 MeV (as for the case of the transverse measurement shown in Fig.5). For this measurement, the Spectrometer dipole was on, while the transverse deflecting cavity was off. The total r.m.s. energy spread calculated on the energy projection of the distribution in the figure was 9.4 keV. Such value includes the contribution of the finite resolution of the spectrometer (that for this measurement was evaluated as $\sim$ 5 keV) and an increase due the residual space charge forces that simulations evaluated to be as high as 50-60%. Accounting for all these contributions, the total r.m.s. energy spread during the measurement can be estimated to be $\lesssim$ 5.3 keV. This value for the total spread is already very close to the goal for the high-order r.m.s. energy spread shown in Table II. Hence, it is reasonable to assume that the high-order r.m.s. energy spread of the measured beam, which is by definition smaller than the total one, is consistent with the estimated value of $\sim$ 5 keV claimed in Table II.

IV. SIMULATIONS

In the first part of this section, the effects of residual space charge forces on the results described in the previous section are evaluated, and in the second part, the experimental results are compared with simulation predictions.

A. Space charge force effects on measurements

The intensity of space charge forces within a relativistic electron beam scales inversely with the square of the beam energy, and to make such forces negligible, energies of $\gtrsim$ 100 MeV at the exit of an electron injector are typically necessary. APEX is located in a preexisting shielded area that is too small to house a 100 MeV injector, with radiation shielding capability insufficient to operate at those energies. Budget limitations prevented relocation or construction of a new high energy test facility. As a reasonable compromise, APEX was designed to deliver beams with a final energy greater than 25 MeV where simulations indicated that the residual space charge forces would be small enough to marginally

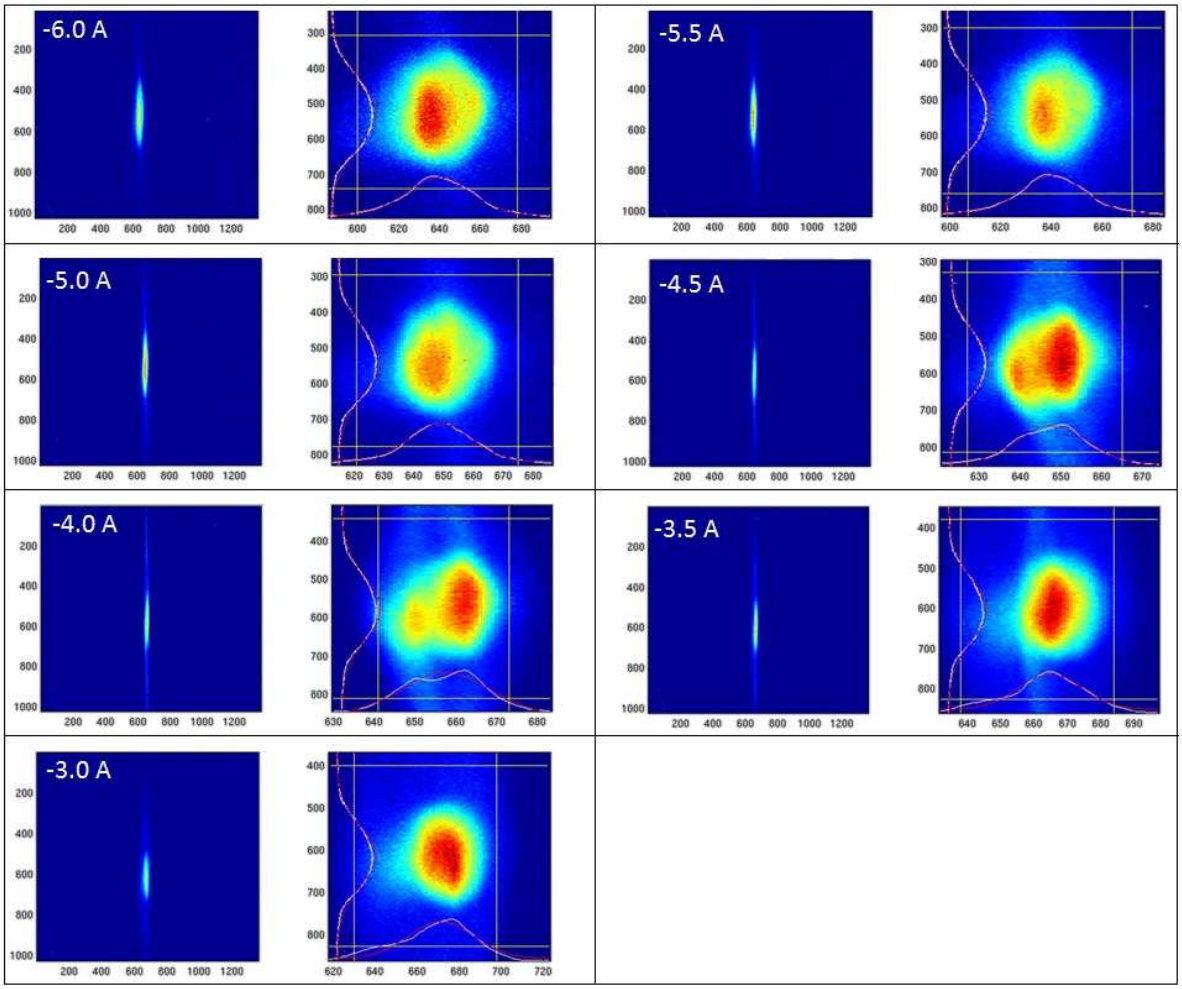

FIG. 8. Details of the horizontal quadrupole scan measurement shown in Fig. 5. Similarly to Fig. 6 case, also here the figure is divided in multiple parts each showing for a different quadrupole current setting the raw beam image in the left side, and the magnification of the area occupied by the beam in the right side. The units for the image axes are pixels (pixel size 16.19 μm).

affect the measurement results. As mentioned earlier in Section II, due to schedule constraints, we were forced to install only two out of the three originally intended sections. In this configuration, the maximum achievable beam energy at APEX was reduced to $\lesssim 17$ MeV. The effects at these energies of residual space charge forces on the measurements described in the previous section are now evaluated.

Figure 11 shows a simulation of a projected emittance measurement using the quadrupole scan technique. Firstly, using the ASTRA code [43] with both space charge forces and higher order field components on, a 20 pC beam was accelerated to 15.5 MeV and compressed to a peak current of ~ 5 A in the APEX linac, and then transported up to the Quad 3 entrance (refer to Fig. 1 for component positions). In the simulation, the APEX parameters were set to the values used during the experiments described in Section III. The simulated emittance value obtained at the entrance of Quad 3 was 0.17 μm. The beam distribution obtained at the entrance of the same quadrupole was then used as input for two different sets of simulations transporting the beam from the Quad 3 entrance to the Screen 3 location using the code IMPACT-Z [44]. In both cases, the Quad 3 current was varied to simulate a quadrupole scan measurement and the resulting transverse images at the screen were recorded. One of the scans was performed turning space charge forces off in the code, the other with space charge forces on. The results were then analyzed with the same routine used during the actual measurements at APEX to extract the emittance value for each of the two cases. Figure 11 shows in the upper part that without space charge forces, the value of the measured emittance coincides, as expected, with the 0.17 μm value obtained at the entrance of Quad 3. The lower part of Fig. 11 shows instead that when space charge forces are on, the analyzing routine does not fit the data properly and the measured emittance value is $\sim 55\%$ higher than the original emittance at Quad 3. This result confirms that, at the energy of the APEX measurements, space charge forces significantly affect the quad scan results, generating a relevant overestimation of the value measured for the emittance.

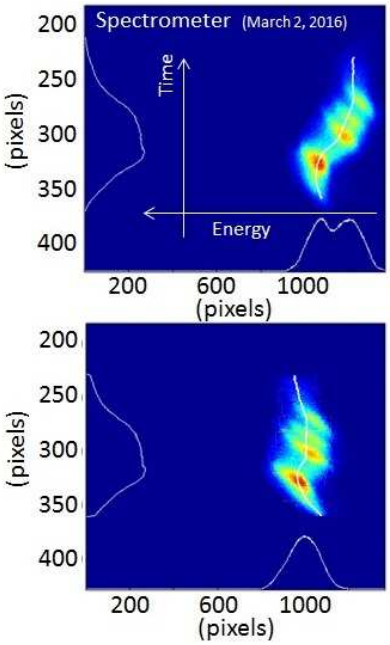

FIG. 9. Example of longitudinal phase space measurement, performed on a 20 pC beam with $\sim$ 5.2 A peak current and 16.2 MeV, obtained using the Transverse Deflecting Cavity in combination with the Spectrometer Dipole and the Spectrometer Screen (see Fig. 1 for component positions). The upper figure shows the row image of the longitudinal phase space at the screen, and the lower figure contains the same image after the linear and quadratic correlations between the energy and time axes have been removed (see text for more details). Calibrations for the temporal and energy axes are 58.9 fs/pixel and 0.20 keV/pixel respectively.

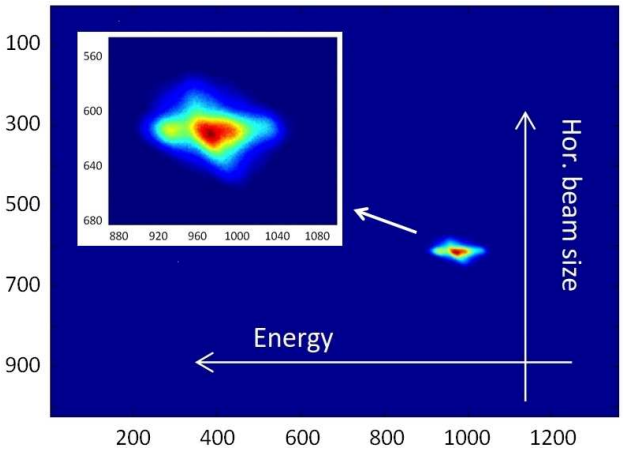

FIG. 10. Example of energy spread measurement, performed on a 20 pC beam with $\sim$ 6 A peak current and 15.7 MeV, The figure shows the image of the beam at the Spectrometer Screen (and its magnification in the inset) when the Spectrometer dipole is on and the Transverse Deflecting Cavity is off (see Fig. 1 for component positions). The units for both axes are pixels with calibration factors of 0.20 keV/pixel and 15.8 μm/pixel for the energy and horizontal axes respectively.

Figure 12 shows the result of an analogous simulation

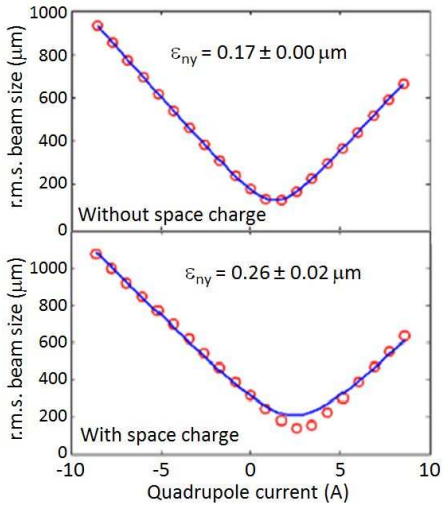

FIG. 11. Results of a simulation of a projected emittance measurement using the quadrupole scan technique. With reference to Fig. 1 for the position of the beamline components, the top part of Fig. 11 shows the case where the beam was propagated from the exit of Quad 3 to the Screen 3 position with space charge forces in the code off. The bottom part shows instead the case when the same beam was transported over the same distance this time with space charge forces on. See the text for a detailed analysis of the results.

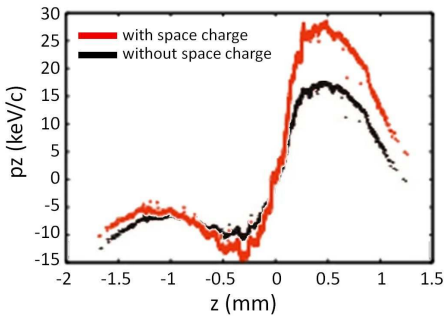

FIG. 12. The figure shows the result of a simulation study investigating the effects of residual space charge forces on the longitudinal phase space measurements performed at APEX. The longitudinal phase space distributions at the Spectrometer Screen for the cases with space charge forces on (in red) and off (in black) are shown. See text for discussion.

study investigating this time the effects of residual space charge forces on the longitudinal phase space. Similarly to the transverse case, a 20 pC beam was compressed to a peak current of $\sim$ 5 A and accelerated at the exit of the second linac section to 15.5 MeV using the ASTRA code with space charge forces on. The beam distribution obtained at this point was then used as input for two additional distinct simulations propagating the beam from the end of the linac to the Spectrometer Screen with space charge respectively on and off. The longitudinal phase space at the Spectrometer Screen for the two cases, visible in Fig. 12, show a clear difference between the distributions. While the bunch current den-

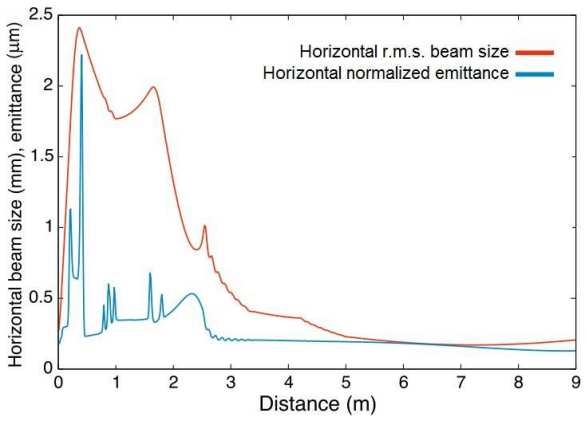

FIG. 13. ASTRA simulation results using the settings showed in Table III. The figure shows the evolution along the APEX beamline of the horizontal normalized emittance and of the horizontal r.m.s. transverse beam size. Because of the cylindrical symmetry of the beamline (the quadrupoles were off in the simulation), the curves for the vertical and horizontal plane cases are identical.

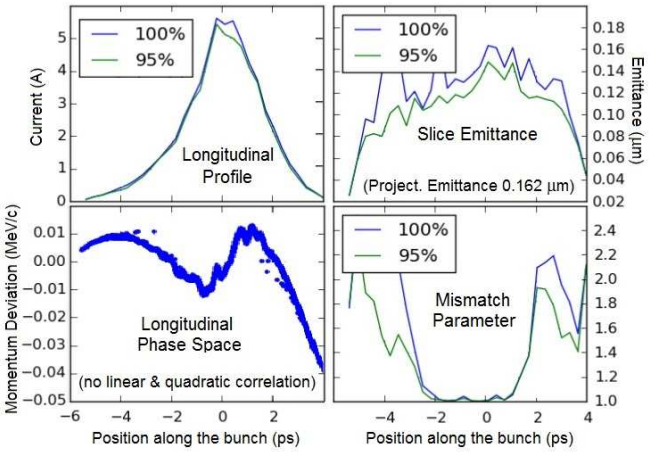

FIG. 14. ASTRA simulation results using the settings showed in Table III and showing the characteristics of the beam predicted at the end of the APEX beamline. See text for more discussion.

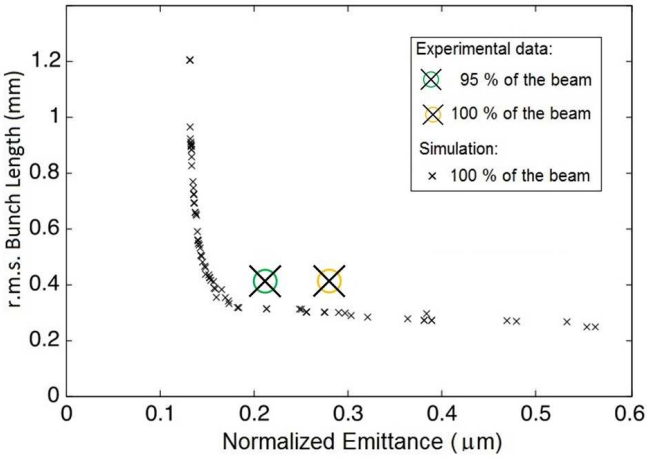

FIG. 15. The small black crosses in the figure show the result of a multi-objective genetic algorithm (MOGA) optimization where transverse normalized emittance and bunch length at the end of the APEX beamline were simultaneously minimized for a 20 pC beam. The two crossed circles are the experimental results discussed in Section III for the 95% and 100% of the beam cases.

sity between the two cases differs only marginally, the particle momentum spread is much larger under the action of space charge forces. Quantitatively, the r.m.s. slice energy spread, the r.m.s. projected energy spread, and the high-order r.m.s. energy spread go respectively from 0.6 keV, 10.6 keV, and 5.8 keV for the no space charge force case, to 1.0 keV, 15.7 keV, and 9.2 keV values when space charge forces are on. Similarly to the transverse phase space case, measurements at the APEX energies generate significant overestimated values also for the longitudinal plane and in particular, the simulation indicates an overestimate in the APEX measurement of the high-order r.m.s. energy spread of ~ 60 %.

B. Experimental results versus simulation predictions

In the last part of this section, the experimental results described in Section III are compared with the simulation predictions obtained using the actual APEX settings utilized during the measurements. In Table III the values used during the experiments and for the simulations are summarized and compared. Due to the limited period available for the beam tests, an accurate and systematic evaluation of the experimental errors was not performed. An estimate of the uncertainty in the values for the different quantities showed for most of them an experimental error contained within a few percent level. Notable exceptions were represented by the case of the buncher and linac sections voltages, where the uncertainty approached values as high as 10%. The laser pulse shape, rise and fall times were not directly measured and their nominal values are shown in Table III.

The experimental settings were used as input for the simulations, and only a couple of them were tweaked to better match the final experimental results. Table III shows that such adjustments were all minimal with the exception of the buncher RF phase that was set for the simulation at 22 RF degrees instead of the measured 55 degrees. The larger phase value indicates a buncher imprinting less energy-to-longitudinal position correlation but providing a larger net acceleration to the bunch. The discrepancy between the two values could be explained by the uncertainty on the actual value of the energy gain in the linac sections and the buncher, and by the fact that the simulation constrained the energy at end of the linac to match the value measured during the experiment. In this situation, a de-phasing of the buncher RF could have

TABLE III. Comparison between the parameter values used in the simulation showed in Figs. 13 and 14 and the ones used in the esperiment.

Parameter and units	Experimental settings	Simulation settings
Laser pulse shape	Trapezoidal*	Trapezoidal
Laser pulse flat top (ps)	28*	28
Laser pulse rise and fall time (ps)	2*	2
Laser transverse shape	1-σ truncated Gaussian	1-σ truncated Gaussian
Laser transverse r.m.s. radius (μm)	170	170
Bunch charge (pC)	20	20
Buncher voltage (kV)	173	175
Buncher RF phase from zero crossing (RF deg @ 1.3 GHz)	50	22
Gun and Linac sections RF phase	on crest	on crest
Solenoid 1 current (A)	4.1	4.11
Solenoid 2 current (A)	2.7	2.68
Beam energy at the VHF-Gun exit (keV)	630	630
Beam energy at the Linac exit (MeV)	15.7	15.7
CsK_2Sb cathode thermal emittance (μm/mm r.m.s.)	0.6	0.6

*Estimated.

been introduced to provide an extra energy boost.

Figure 13 shows the evolution along the APEX beamline of the transverse normalized emittance and of the r.m.s. transverse beam size obtained by the ASTRA simulation using the values in Table III as input. The emittance curve indicates a well-performed emittance compensation process. Figure 14 shows instead the simulated beam characteristics at the end of the APEX beamline. The results for 100% and 95% of the particles are shown for the beam longitudinal profile (which is consistent with the measured one shown in Fig. 4) and for a slice emittance fairly equally distributed along the bunch slices. Also shown is the mismatch parameter [45] that indicates how the emittance ellipses calculated for each of the longitudinal slices of the beam are aligned in the transverse phase space. A properly done emittance compensation aligns all the ellipses and results in a mismatch parameter value of 1. The almost perfect value shown by the simulation for such a quantity in the core of the beam confirms, as previously noted, a successful emittance compensation process. The longitudinal phase space is shown after the linear and quadratic correlations between the particle momentum and longitudinal position are removed. This is done based on the assumption (discussed and justified in Section III C) that only higher order correlations limit the linac compression performance and require attention and a minimization effort already at the injector. Overall, the values of the simulated emittance and of the high-order r.m.s. energy spread are consistent with the experimental results when the space charge effects associated with the measurements are included as described in the previous sub-section.

The analysis of the experimental results discussed in Section III already pointed out that the APEX subsystems were not optimally set during the measurements (presence of laser halo, beam misalignment along the linac, non optimized bunch longitudinal profile, etc.). That observation leads to the question: how far are the results of the measurements from those achievable by a fully optimized APEX beamline? An answer can be provided by comparing the experimental data with the results of a multi-objective genetic algorithm (MOGA) optimization [46] where the transverse normalized emittance and the bunch length of a 20 pC beam are simultaneously minimized at the end of the APEX beamline. Figure 15 shows the result of this optimization, in which the beamline parameters were allowed to vary to find the so-called Pareto front [46], the set of trade-off solutions (small black crosses in the figure) where each solution is better than any other in one of the optimized quantities. Also shown in Fig. 15 by crossed circles, are the experimental results discussed in Section III for the 95% and 100% of the beam cases. Both of the experimental points do not lay on the Pareto curve and they show larger emittance values with respect to the fully optimized, same bunch length solution in the Pareto front. This observation remains true even when the space-charge induced over-estimation previously described is accounted for. This is an additional confirmation that, although the APEX experimental results presented in this paper already demonstrated all the requirements for driving an x-ray FEL, a further optimization of the beamline has the potential to significantly improve the overall quality of the beam.

V. CONCLUSIONS

The VHF-Gun, a novel scheme RF photo-gun, was conceived, designed and fabricated at the Lawrence Berkeley National Laboratory (LBNL) in response to the need of an electron source capable to drive an x-ray FEL at MHz-class repetition rates. A two-month measurement campaign at the APEX injector test facility at LBNL was dedicated to verify the capability of the VHF-Gun

of generating such electron beams.

As reported in this paper, in spite of schedule constraints that prevented performing a systematic and full optimization of the APEX injector, all targeted goals were successfully demonstrated. The analysis of the results also indicated that additional performance improvements can be achieved by a further tuning and optimization of the parameters. Finally, the overall agreement between experimental and simulated results reinforces the confidence on the simulation tools used and hence the credibility of the results that simulations predicts for the VHF-Gun operated at other charges per bunch [47].

As a consequence of these positive results and of the operational reliability previously demonstrated by the gun, several proposed and in construction FEL facilities are planning to use a VHF-Gun as their electron source. In particular, a second VHF-Gun was built at LBNL and delivered to SLAC to drive the LCLS-II, the high-repetition rate x-ray FEL in construction at Stanford. The original VHF-Gun continues to operate at full time at LBNL as the electron source for HiRES the LBNL ultra-fast electron diffraction experiment.

VI. ACKNOWLEDGEMENTS

The authors want to thank the management and personnel of the Advanced Technology Applied Physics, Advanced Light Source and Engineering divisions at the Lawrence Berkeley National Laboratory for their continuous support during all phases of the APEX project.

Work supported by the Director of the Office of Science of the U.S. Department of Energy under Contract No. DE-AC02-05CH11231.

[1] J. M. J. Madey, *Journal Appl. Phys.* **42**, 1906-1913.
[2] P. Emma, *et al.*, *Nature Photonics* **4**, 641-647, (2010).
[3] T. Ishikawa, *et al.*, *Nature Photonics* **6**, 540, (2010).
[4] H. H. Braun *Proceedings of the 2012 Free Electron Laser Conference, Nara, Japan (2012)*, pp. 9.
[5] J.-H. Han, H.-S. Kang, and I. S. Ko, *Proceedings of the 2012 International Particle Accelerator Conference, New Orleans, LA, USA (2012)*, pp. 1735.
[6] H. Weise, and W. Decking, *Proceedings of the 2017 Free Electron Laser Conference, Santa FE, NM, USA (2017)*, pp. 9.
[7] W. Ackermann, *et al.*, *Nature Photonics* **1**, 336, (2007).
[8] S. Di Mitri, *et al.*, *Proceedings of the 2011 International Particle Accelerator Conference, San Sebastian, Spain (2011)*, pp. 918.
[9] See for example: C. Limborg-Deprey, D. Dowell, J. Schmerge, Z. Li, and L. Xiao, *RF Design of the LCLS Gun*, LCLS TN-05-3, February 2005, or, S. Rimjaem, *et al.*, in Proceedings of the 2009 FEL Conference, Liverpool, UK, August 23-28, 2009, p. 251.
[10] See for example: E. Arenholz, *et al.*, *Toward Control of Matter: Basic Energy Science Needs for a New Class of X-Ray Light Sources*, Proc. of the Science for a New Class of Soft X-Ray Light Sources Workshop, Berkeley, CA, October 8-10, 2007, LBNL Report LBNL-1034E (September 24, 2008). (available at http://www.osti.gov/scitech/biblio/941167)
[11] J. Sekutowicz,*et al.*, *Proceedings of the 2013 Free Electron Laser Conference, New York, NY, USA (2013)*, pp. 189.
[12] J. Corlett,*et al.*, *Synchrotron Radiation News* **22**, No. 5, 25 (2009).
[13] J. Bisognano, *et al.*, *Proceedings of the 2009 Particle Accelerator Conference, Vancouver, BC, Canada (2009)*, pp. 109.
[14] R. Bartolini, *et al.*, *Proceedings of the 2009 Free Electron Laser Conference, Liverpool, UK, (2009)*, pp. 490.
[15] K.-J. Kim, S. Reiche, Y. Shvydko, *Phys. Rev. Letters* **100**, 244802 (2008).
[16] J. Galayda, *Proceedings of the 2014 International Particle Accelerator Conference, Dresden, Germany (2014)*, pp. 935.
[17] Shanghai Coherent Light Facility (SCLF) Pre-Conceptual Design Report, August 7, 2017.
[18] J. W. Staples, S. P. Virostek, and S. M. Lidia, *Proceedings of the 2004 European Particle Accelerator Conference, Lucerne, Switzerland, (2004)*, pp. 473.
[19] F. Sannibale, *Proceedings of the 2016 North America Particle Accelerator Conference, Chicago IL, USA (2016)*, pp. 445.
[20] J. Staples, F. Sannibale, and S. Virostek, CBP Tech. Note 366, 2006, LBNL-1003792, available at https://publications.lbl.gov/publication_search.
[21] F. Sannibale, *et al.*, *Phys. Rev. ST - Accel. and Beams* **15**, 103501 (2012)
[22] R. Wells, *et al.*, *Rev. of Sci. Instr.* **87**, 023302 (2016).
[23] R. Huang,*et al.*, *Phys. Rev. ST - Accel. and Beams* **18**, 013401 (2015).
[24] D. Filippetto, H. Qian, and F. Sannibale, *Appl. Phys. Lett.* **107**, 042104 (2015).
[25] F. Sannibale, D. Filippetto, and C. F. Papadopoulos, *Journal of Modern Optics* **58**, 1419 (2011).
[26] F. Sannibale. *Nuclear Instruments and Methods in Physics Research A* **740**, 10-16 (2014).
[27] D. Filippetto, and H. Qian, *Journal Phys. B: At. Mol. Opt. Phys.* **49**, 104003 (2016).
[28] F. Sannibale, *et al.*, *Phys. Rev. Accel. and Beams* **20**, 113402 (2017).
[29] Z. Ding, *et al.*, *Phys. Rev. Accel. and Beams* **20**, 113401 (2017).
[30] I. V. Bazarov, B. M. Dunham, C. K. Sinclair, *Phys. Rev. Letters* **102**, 104801 (2009).
[31] D. Filippetto, P. Musumeci, M. Zolotorev, and G. Stupakov, *Phys. Rev. ST - Accel. and Beams* **17**, 024201 (2014).
[32] D. Sertore, S. Schreiber, K. Floettmann, F. Stephan, K. Zapfe, and P. Michelato, *Nucl. Instrum. Meth. A* **445** (2000) 422–426.
[33] S. P. Virostek, F. Sannibale, J. W. Staples, H. J. Qian, *Proceedings of the 2017 International Particle Accelerator Conference, Copenhagen, Denmark, (2017)*, pp. 473.
[34] J. Power, *et al.*, *Proceedings of the 2010 International*

Particle Accelerator Conference, Kyoto, Japan, (2010), pp. 4310.

[35] H. Qian, *et al.*, *Proceedings of the 2013 National Particle Accelerator Conference, Pasadena, CA USA, (2013)*, pp. 607.

[36] D. Filippetto, *et al.*, *Proceedings of the 2012 International Particle Accelerator Conference, New Orleans, LA, USA (2012)*, pp. 963.

[37] S. Belomestnykh, *et al.*, *Nuclear Instruments and Methods in Physics Research A* **614**, 179 (2010).

[38] J. Schmerge, *LCLS-II Engineering note* LCLSII-2.3-EN-0391-R3, September 29, 2016.

[39] T. Vecchione, *et al.*, *Applied Physics Letters* **99**, 034103, (2011).

[40] See for example: H. Wiedemann, *Particle Acelerator Physics*, Springer, 3rd Edition, 2007.

[41] G. A. Loew, O. H. Altenmueller, *Design and applications of RF deflecting structures at SLAC*, SLAC PUB-135, August 1965.

[42] D. H. Dowell, T. D. Hayward, and A. M. Vetter, *Proceedings of the 1995 Particle Accelerator Conference, Dallas, TX, USA (1995)*, pp. 992.

[43] K. Flottman, http://www.desy.de/∼mpyflo/.

[44] J. Qiang, http://amac.lbl.gov/ jiqiang/IMPACT/.

[45] See for example: E. Prat, *et al.*, *Phys. Rev. ST Accel. Beams* **17**, 104401 (2014).

[46] K. Deb, *Multi-Objective Optimization using Evolutionary Algorithms*, Wiley (2001).

[47] See for example: C. Mitchell, *et al.*, *Proceedings of the 2016 International Particle Accelerator Conference, Busan, Korea (2016)*, pp. 1699.